Research Article

Chenxi Shi, Shibin Liu, Irfan, Qinglin Gong, Huan Wang, and Ming Hu*

Deposition mechanisms and characteristics of nano-modified multimodal Cr_3C_2–NiCr coatings sprayed by HVOF

https://doi.org/10.1515/rams-2022-0042
received March 07, 2022; accepted May 25, 2022

Abstract: Nano-modified multimodal and conventional Cr_3C_2–NiCr coatings were fabricated by high-velocity oxygen-fuel spraying deposited on CuCrZr substrates. Results showed that individual nano-modified multimodal Cr_3C_2–NiCr particles were composed of nano (25–180 nm), submicron (200 nm to 0.5 μm), and micron (2–4.5 μm) Cr_3C_2 grains, NiCr binder phases, and a tiny amount of rare earth oxide additives. The nano-modified multimodal Cr_3C_2–NiCr coatings maintained a unique structure: submicron Cr_3C_2 grains embedded in the voids formed by micron Cr_3C_2 grains, NiCr binder phases and nano Cr_3C_2 grains imbedded in the voids formed by submicron and micron Cr_3C_2 grains, and nano Cr_3C_2 grains are dispersed in NiCr metal binder phases. A few discontinuous elongated amorphous and nanocrystalline phases existed in them. The mechanical interlocking was the dominant bonding mechanism accompanied by local metallurgical bonds. Compared to the conventional coating, the multimodal coating was uniform and dense (porosity was 0.3 ± 0.12%) as well as not obvious lamellar structures, the adhesive strength was 75.32 ± 1.21 MPa, exhibiting a 65 pct increase, and the microhardness was increased by about 18%. The lower porosity and higher strength of nano-modified multimodal structure coating were mainly related to dispersion distribution and synergistic coupling effects of Cr_3C_2 hard grains with different scales.

Keywords: multimodal microstructure, HVOF, nano-modified, Cr_3C_2–NiCr coatings, characteristics, depositing mechanism

1 Introduction

Thermal spraying technology finds application in aerospace, automobile, textile, and mining industrial fields. The high-velocity oxygen-fuel (HVOF) deposition process, due to its high velocity and low temperature, is generally used to deposit metallic and cermet coatings [1]. The deposition of coating shows a minor structural change with a reasonable structural density during coating fabrication by the HVOF spraying technique [2]. With high impact velocities of the particles, the coatings of HVOF spraying demonstrate superior performances, such as low porosity, high density, hardness, and bonding strength [2].

The conventional Cr_3C_2–NiCr coatings have been employed to apply carbide cermet coating on industrial equipment due to its excellent resistance to wear, erosion, thermal shock, and high-temperature stability in the thermal spray community. Nowadays, researches on conventional Cr_3C_2–NiCr coatings have mainly focused on their properties, such as tribological properties [3–5] and corrosion resistance [6,7]. Other investigations have included studying manufacturing technologies of sprayed conventional Cr_3C_2–NiCr coatings [8–12]. The properties of these coatings have depended on primary factors including the variety of deposition methods (parameters) and the microstructure of coatings. However, the performances of conventional

* **Corresponding author: Ming Hu,** Jiamusi University College of Materials Science and Engineering, Jiamusi, 154007, China; Metal Wear Resistant Materials and Surface Technology Engineering Research Center in the Ministry of Education, Jiamusi, 154007, China, e-mail: minghu02@163.com
Chenxi Shi: Jiamusi University College of Materials Science and Engineering, Jiamusi, 154007, China, e-mail: shichenxi991@126.com
Shibin Liu: Jiamusi University College of Materials Science and Engineering, Jiamusi, 154007, China; Metal Wear Resistant Materials and Surface Technology Engineering Research Center in the Ministry of Education, Jiamusi, 154007, China, e-mail: jmsdxliu@126.com
Irfan: Jiamusi University College of Materials Science and Engineering, Jiamusi, 154007, China, e-mail: irfankhanswabi20@gmail.com
Qinglin Gong: Jiamusi University College of Materials Science and Engineering, Jiamusi, 154007, China, e-mail: 88572355@qq.com
Huan Wang: Jiamusi University College of Materials Science and Engineering, Jiamusi, 154007, China, e-mail: 718515347@qq.com

Cr_3C_2–NiCr coatings seemed to have certain limitations and were generally difficult to breakthrough.

Some researchers have showed that small additions of the Cr_3C_2–NiCr coating improved its properties [13–16]. Matthews et al. [17] have explored a novel method to improve the properties of Cr_3C_2–NiCr coatings. Besides, some studies have focused on the nanostructured Cr_3C_2–NiCr coatings [18,19]. In contrast, the nanostructured coatings were challenging to retain the nanostructural features of original powders due to too high spraying temperature and/or too long dwell times, causing the partial or total loss of the nanostructural character [20]. This needs to monitor in-flight particle temperature and velocity but increases the production cost. Due to fewer defects, the properties could be improved perfectly by introducing the fine fillers in the conventional coatings [21]. In recent years, some researchers have reported bimodal and multimodal structure carbide cermets coatings of the same type, such as WC-Co and TiC-Fe [22–28].

To overcome the problem of the property limitations of conventional Cr_3C_2–NiCr coatings and reduce processing costs, the nano-ceramic coating team of professor Wang You of the nano surface engineering laboratory of the Harbin University of Technology has developed a nano-modified multimodal structure Cr_3C_2–NiCr powder. There are limited studies on the microstructure, depositing mechanisms, and performance of nano-modified multimodal Cr_3C_2–NiCr coatings, and the potential of these coatings needs further research and development.

In this present study, the nano-modified multimodal and conventional Cr_3C_2–NiCr coatings prepared on CuCrZr by HVOF spraying have been investigated. The microstructure features, phase composition, and mechanical properties of both coatings have been comparatively studied. Finally, the depositing mechanisms of the multimodal Cr_3C_2–NiCr coatings have been researched in detail.

2 Experimental procedure

2.1 Materials

In the present work, two kinds of Cr_3C_2–NiCr powders were used as feedstock, namely, conventional Cr_3C_2–NiCr powders (Chongyi ZhangYuan Tungsten Co., Ltd.) and nano-modified multimodal Cr_3C_2–NiCr powders (Fujian Dilon Innovation Development Co., Ltd.), marked as CP and MP, respectively. The powder size exhibited dimensions and distributions of 15–45 μm. The obtained coatings were marked as CC and MC, respectively.

2.2 HVOF spraying process

The CuCrZr substrates were ultrasonically cleaned with acetone and sandblasted with Al_2O_3, then subsequently cleaned with pressurized air and preheated over 200°C before spraying. The CP and MP were deposited on CuCrZr substrates using an HVOF spraying system (HV-80-JP), and the average thickness of the coating was 200 μm. The optimized spraying parameters are summarized in Table 1.

2.3 Microstructural characterizations

Scanning electron microscopy (SEM; SU8020, HITACHI, Japan) was used to observe the morphology and microstructure of the powders, the original surfaces, and polished cross sections of the coatings, and the corresponding element distribution was analyzed by energy-dispersive spectroscopy (EDS; Super X, FEI, USA). The proportion of nano, submicro, and micro grains was obtained by selecting random 20 magnification of 5000× SEM microphotographs of powders, calculating the area of each size and taking the average value. The porosities of the coatings were evaluated by using Image-Pro® Plus v 6.0. In this case, at ten magnification of 500×, polished cross-sectional SEM microphotographs were taken randomly and the average value was calculated. For the investigations of the phases composition, the feedstock particles and the polished surfaces of coatings were characterized by the X-ray diffraction (XRD; UltimaIV, Rigaku, Japan) employing Cu-K_α radiation (λ = 1.5418 Å) at 40 kV, 40 mA and 0.02°/step, the scanning rate was 8°/min with the range of $20° \le 2\theta \le 100°$. The crystallographic structures of the nano-modified multimodal Cr_3C_2–NiCr coatings were further characterized by high-resolution transmission electron microscopy (TEM;

Table 1: HVOF spraying parameters of as-sprayed Cr_3C_2–NiCr coatings

Parameters	Value
Fuel type	Kerosene
Fuel flow rate ($l{\cdot}min^{-1}$)	19–23
Oxygen flow rate ($l{\cdot}min^{-1}$)	40–53
Powder feed rate ($g{\cdot}min^{-1}$)	50–70
Carrier gas type	N_2
Carrier gas flow rate ($l{\cdot}min^{-1}$)	7
Stand-off distance (mm)	250–320
Number of cycles	10

Tecnai G2 F30, FEI, USA), and the TEM samples were prepared by the focused ion beam.

2.4 Mechanical properties evaluations

The resulting coatings were evaluated concerning their microhardness and adhesive strength. The cross-sectional microhardness of the coating was carried out using the microhardness tester (HVT-1000A, Shandong shancai Test Instrument, China) with an applied load of 300 g ($HV_{0.3}$) and a hold time of 15 s. To obtain the stability of the data, the microhardness was based on the average value for random 12 points in different areas. The adhesive strength of the coating was tested by a universal tensile test machine, and the values were the average of three samples.

3 Results and discussion

3.1 Characterization of the feedstock powders

3.1.1 Powder morphology

The Cr_3C_2–NiCr feedstock powders were characterized with respect to their particles' morphology and shape, microstructure, apparent density, composition and elements distribution, and phase analysis. Figure 1 illustrates the SEM micrographs of CP and MP.

It can be seen that CP exhibits highly spherical morphology (Figure 1a), indicating the good flow ability during the HVOF process, and MP exhibits irregularly crashed disk agglomerates (Figure 1d). This morphology is attributed to the continuous collisions of the ball and the particles inducing severe deformation during the mechanical milling. By viewing the powders at higher magnification, it is possible to observe that CP has relatively smooth surfaces (Figure 1b), the surface of MP is surrounded by fine grains, typical of an agglomerated and sintered powder (Figure 1e). Figure 1c and f present cross-sectional views of the feedstock powders. CP shows many voids (Figure 1c), and MP appears a homogenous and dense microstructure (Figure 1f), which modifies with the densification treatments. The structure in the interior of MP consists of micron and submicron carbide grains embedding into the metal binder phases. The agglomerated nano-sized grains fill in the voids of MP, which contribute to obtaining dense coatings, as illustrated in the rectangle ① in Figure 1f. The outer layer of MP is surrounded by a NiCr binder shell (rectangle ② contains primarily Ni and Cr analysis to be the metallic binder; Table 2) with a wall thickness of 0.5–1 μm, as illustrated in the rectangle ② in Figure 1f.

Figure 2 presents the partial outside view of individual powder. As can be seen, the original crystal grains of individual CP particles consist of micro-size (2–4.5 μm)

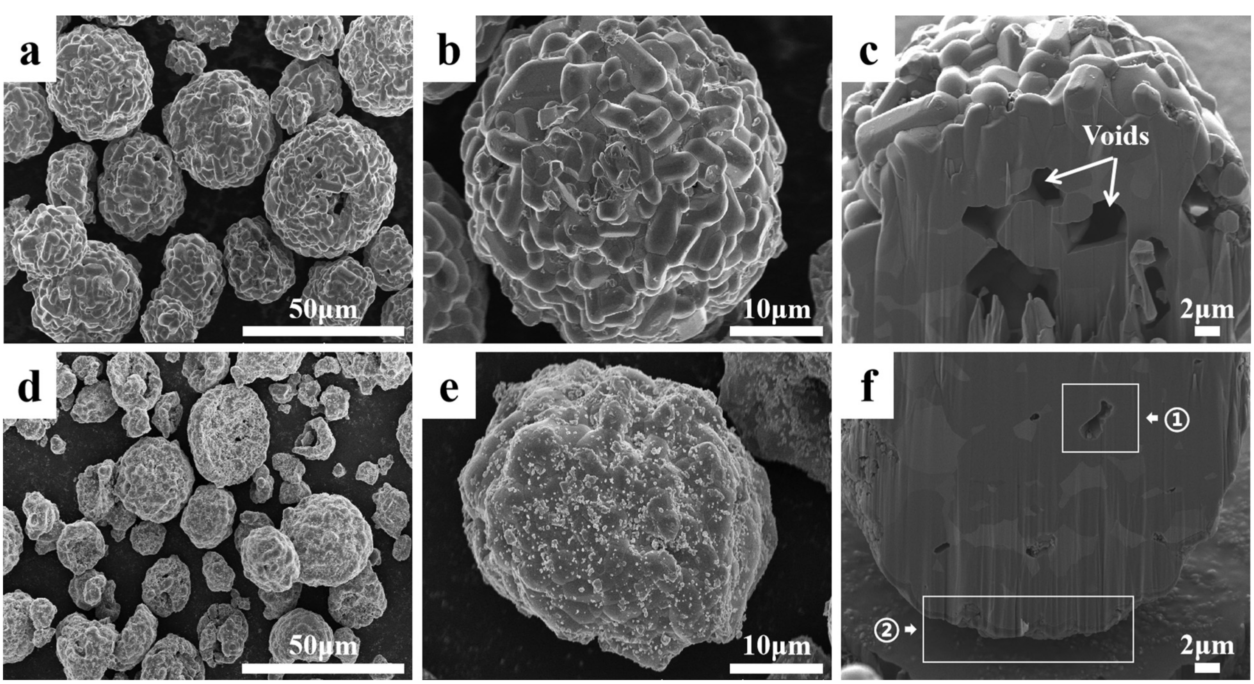

Figure 1: SEM images of Cr_3C_2–NiCr powders: (a, b, c) CP; (d, e, f) MP.

Table 2: Elemental composition of specific regions of Cr_3C_2–NiCr powders (wt%)

		C	Cr	Ni	REO	Others
CP	Coarse grains	7.44	91.27	0.96	0.00	0.33
	(like A)	14.87	83.98	0.92	0.00	0.23
		11.34	87.26	1.03	0.00	0.37
	Fine grains (like B)	10.78	88.16	1.02	0.00	0.04
		11.19	85.34	3.39	0.00	0.08
		14.57	81.51	3.72	0.00	0.20
MP	Coarse grains	12.21	85.30	1.26	1.08	0.15
	(like C)	3.59	86.70	1.56	7.81	0.34
	Coarse grains	3.96	77.19	3.32	15.34	0.19
	(like D)	14.95	81.39	1.48	2.09	0.09
	Fine grains (like E)	12.76	85.14	1.23	0.68	0.19
		9.38	85.47	1.55	3.28	0.32
	Rectangle ②	1.60	16.65	77.39	4.16	0.20
		3.77	49.52	43.85	2.59	0.27
		6.55	59.47	26.12	7.68	0.18

(Figure 2a), while the original crystal grains of individual MP particles are composed of 11.5 wt% nano grains (25–180 nm), 34.6 wt% sub-micro grains (200 nm to 0.5 μm), and 53.9 wt% micro grains (2–4.5 μm; Figure 2b).

According to the EDS results (Table 2), CP consists mainly of C, Cr, and Ni, and this is the same chemical composition as MP, but MP contains rare earth oxide additives. As is well known, the rare earth oxide additives possess an active chemical property and sizeable atomic radius [16]. Consequently, it is generally induced segregations on the surface of the grain and inhibits the grain heterogeneous growth. Moreover, adding REO also can accelerate the dissolution of the hard reinforcement particles, and then a refined microstructure can be formed [16].

The coarse grains (like A) and fine grains (like B) of CP (Figure 2a) contain higher levels of Cr and C; thus, both of the two regions are considered to be the carbides. For the MP (Figure 2b), the coarse grains (like C and D) and fine grains (like E) are greater contents of Cr although a minor amount of Ni exists, indicating the carbides. The formation of the structure can be explained that a large number of carbide particles are fractured and embedded into the metallic binder during the mechanical milling process. Thus, the metallic binder was present in the gaps between fractured carbide particles, giving the result that Ni is observed in the carbides. Similarly, most of the metallic binder is combined with fractured carbide particles. Clearly, the metallic binder was not a completely pure NiCr solid solution, and it contained some carbide particles [18].

Therefore, each MP particle was a multimodal agglomerate, which consisted of micron, submicron, and nano Cr_3C_2 grains, NiCr metal binder phases, and rare earth oxides. It formed a three-layer structure: the inner core was composed of micron and submicron carbide cermet embedded into the metal binder phases, the outer layer was a metal binder shell that surrounded the inner core, and the outermost layer adsorbed with different size submicron and nano Cr_3C_2 grains and rare earth oxides, which covered the metal binder shell.

3.1.2 Phase composition

Figure 3 shows the XRD spectra of the Cr_3C_2–NiCr powders and coatings. As can be observed, Cr_3C_2 and (Cr, Ni) crystalline phases were detected in CP and MP (Figure 3a), which showed a similar phase composition for these two powders. The diffraction intensities of REO additives existing in the crystallographic form were too weak to be detected in MP.

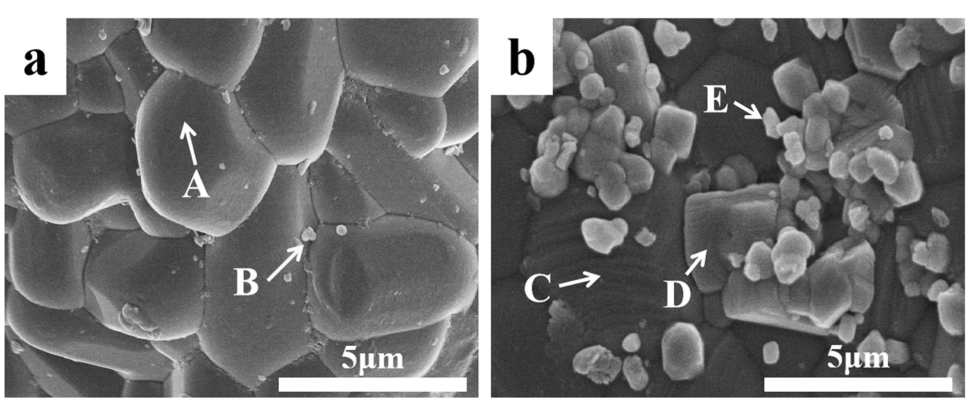

Figure 2: SEM images of Cr_3C_2–NiCr powders: (a) CP and (b) MP.

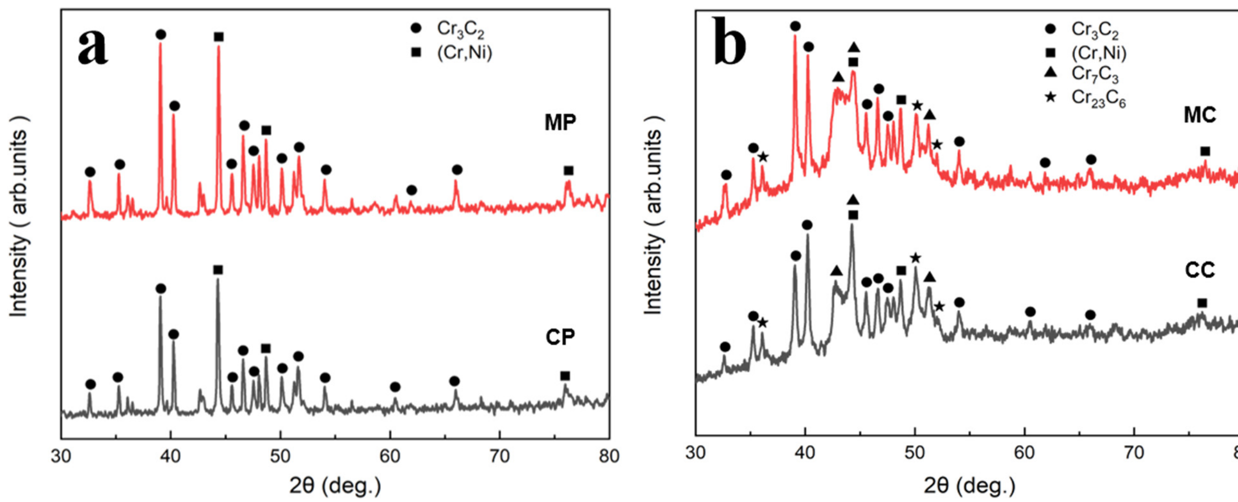

Figure 3: XRD patterns of Cr_3C_2–NiCr powders and coatings: (a) feedstock powders and (b) both the coatings.

3.2 Characterization of the coatings

3.2.1 Phase composition

As shown in Figure 3b, the major diffraction spectra peaks of both the coatings could be associated with Cr_3C_2, Cr_7C_3, $Cr_{23}C_6$, and (Cr, Ni) phases. The ratio between the peak at 40.209° and the highest one at 39.022°, and the relative diffracted peak of Cr_3C_2 phase in MC (0.90) were significantly lower than for CC (1.25), which revealed various amounts of decarburization or interdiffusion of carbides in MC [29]. Meanwhile, the diffraction peaks at 42.183–44.835° for MC can be clearly observed broader than the related peaks for CC, indicating the presence of the nonequilibrium microstructure composed of partly amorphous and/or nanocrystalline phases [30]. This might be attributed to the fact that the dissolution of Cr and C could perform in the Ni phase at high temperatures, while it is difficult to crystallize due to the rapid solidification during the HVOF process. Furthermore, its initial nanometric grains of MC can be maintained even after the HVOF spraying due to the lower temperature and shorter residence time [31].

The new diffraction spectra of Cr_7C_3 and $Cr_{23}C_6$ were detected in the two Cr_3C_2–NiCr coatings due to the decarburization of Cr_3C_2, and the diffraction peak overlap at $2\theta = 44.16°$. When in-flight Cr_3C_2 particles were heated by jet flame or during coating formation, the following phase transformations or reactions could occur:

$$7Cr_3C_2 \rightarrow 3Cr_7C_3 + 5C, \quad (1)$$

$$23Cr_3C_2 \rightarrow 3Cr_{23}C_6 + 28C, \quad (2)$$

$$23Cr_7C_3 \rightarrow 7Cr_{23}C_6 + 27Cr, \quad (3)$$

$$C + O_2 \rightarrow CO_2 \quad \text{or} \quad 2C + O_2 \rightarrow 2CO. \quad (4)$$

Liquid–solid reactions occur within cermet particles when the ceramic particle, in the solid state, is partially dissolved in the surrounding liquid metal [32]. The NiCr binder phases could fully melt (melting point of 1,690 K) during the high-temperature flame of HVOF spraying. The metallic chromium (Cr) and carbonium (C) in the outer layer of chromium carbide (Cr_3C_2) particles are wetted by molten liquid NiCr, then dissolved, and rapidly diffused into the liquid nickel. These phenomena are following the Arrhenius law, and the reaction rate increases drastically with the particle superheat [32].

A certain part of the free carbon reacts with oxygen that entrained externally into the molten NiCr phases to form CO gas, and the other part continues to spread toward the surface of the liquid NiCr to react with oxygen in the atmosphere to form carbon oxide gases (CO or CO_2) bleeding to the atmosphere. Therefore, metastable carbides (Cr_7C_3 and $Cr_{23}C_6$) may form at the interface of Cr_3C_2 and NiCr phases. Furthermore, dissolved carbon is lost as CO or CO_2 gases [33], which promotes the formation of Cr_7C_3 and $Cr_{23}C_6$ phases.

3.2.2 Microstructure

Figure 4 observes closely packed particles and predominantly rough surfaces on the top coatings. Such structural features are the typical morphology of thermal spray coatings. The surface particles of MC were finer than CC, as illustrated in Figure 4a–c, those were quite similar to the initial powders. For the case of CC, the as-sprayed coatings were built-up by a certain amount of micron-sized grains (Figure 4b). For the case of MC, submicron Cr_3C_2 grains embedded in the voids formed by micron Cr_3C_2 grains, NiCr binder phases and nano Cr_3C_2 grains imbedded in the voids formed by submicron and micron Cr_3C_2 grains, and nano Cr_3C_2 grains are dispersed in NiCr metal binder phases, those formed the unique multimodal structure coatings (Figure 4d). A magnified region within the rectangle in Figure 4c displays a certain amount of near-globular shape micro grains that form the agglomerate. Such agglomerated reaction might be due to the higher surface-to-bulk ratio and chemical reactivity of the nano-sized particles that lead to a strong surface effect. In addition, partial nano-sized particles connected with each other to promote the formation of larger agglomerates during the Brownian movement. In addition, nano particles with high specific surface areas possessing strong surface tension may be another reason for the agglomerated reaction.

Table 3 lists EDS surface scanning information of Cr_3C_2–NiCr powders and coatings. EDS analysis revealed that both coatings contain small amounts of oxides (not detected peaks in the XRD pattern) and MC oxygen content higher than that of CC, which contains 5.59 (wt%) and 2.30 (wt%), respectively. The presence of oxides might be attributed to the fact that most spray experiments are performed in the atmosphere. On the one hand, the surfaces of the metallic matrix form the oxide regions by preheating, and powders impact the oxide layer existing on the metallic matrix surface. On the other hand, powders also are oxidized both in-flight or during deposition because oxygen in the atmosphere is entrained within the high-energy jet and reacts with the high-temperature particles in-flight. In addition, the oxygen working with HVOF equipment is always excessive, and the residue oxygen may also react with the hot in-flight particles [34].

Furthermore, EDS results of carbon content were investigated: 15.50 (wt%) and 11.96 (wt%) for CC and MC, respectively. Another problem related to carbide

Table 3: Elemental composition of Cr_3C_2–NiCr powders and coatings (wt%)

	C	O	Cr	Ni	REO
CP	71.73	0.00	26.11	2.16	0.00
MP	68.87	0.00	24.09	5.39	1.65
CC	15.50	2.30	56.34	25.87	0.00
MC	11.96	5.59	59.95	21.06	1.44

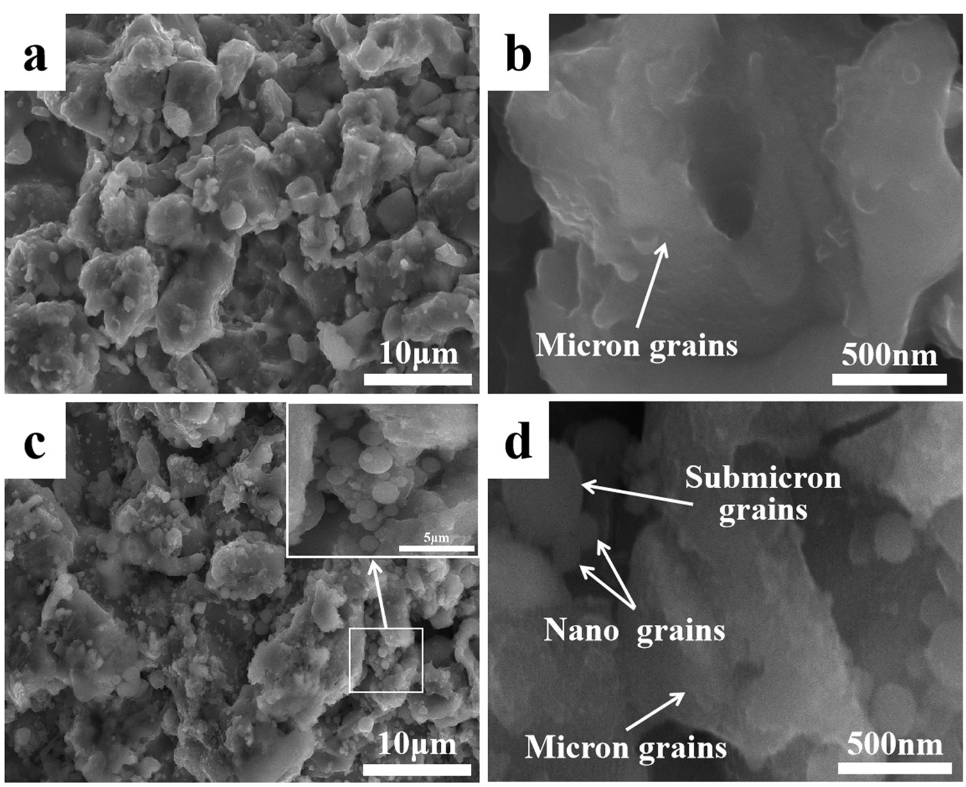

Figure 4: SEM images of Cr_3C_2–NiCr coatings top surface: (a) CC, (b) higher magnification view of CC, (c) MC, and (d) higher magnification view of MC.

cermets coatings is linked to decarburize, especially for nano-sized coating. The degree of decarbonization of MC is higher than that of CC due to the larger surface area-to-mass ratio of the nano-sized particles, even under HVOF spraying conditions.

Figure 5 illustrates the secondary electron images of the cross-sectional microstructure of the two coatings. The low magnifications are exhibited to provide an overview of the cross-sectional coating microstructure (Figure 5a and b). The typical lamellar microstructures of thermal spray coatings exhibit in CC (Figure 5c); however, those are not obviously observed in MC (Figure 5d). The cross sections of both coatings can be observed as cracks and pores, especially in CC. It has been shown that the defects of sintering technology induce the existence of unfilled pores and cracks in Cr_3C_2–NiCr feedstock powders [35,36], and vapors and gases stagnate on the substrates to be sprayed. Moreover, the major defects of lamellar stacking are interlamellar pores [20], and unmelted or resolidified particles remaining in the coating structure may be another source of the pores. In addition, for cermets sprayed with gases that accelerate dissolution in in-flight particles, these gases are not fully released during the short residence times in the jet, thus trapping into the splat [37].

The initiation of the cracks may be attributed to the cracks in powders as mentioned earlier, living in coatings and the lack of melting of NiCr metallic binder, and reduced bonding interfaces, as illustrated in rectangle ① in Figure 5c. In other respects, the cracks are formed by thermal expansion coefficients mismatch between the Cr_3C_2 hard carbides and NiCr metallic binder following the nonequilibrium solidification process, as illustrated in rectangle ② in Figure 5c. In addition, the combination of cohesive failure around peripheral lamellae leads to delaminations between lamellar layers [20]. Finally, owing to the residual stresses generated within coating during manufacturing processes.

As can be seen, the coatings consist of different shading contrast zones of dark gray, medium gray mixture, and light gray, which can be distinguished by contrast lighter and darker in the coating microstructure (Figure 5). Figure 6a–e shows the elemental composition by EDS spectra at selected parts of the dark-gray, medium-gray mixture, and light-gray zones. The dark-gray area of CC contained C and Cr; thus, the dark-gray area was considered to be carbides. The light-gray area observed C, Cr, and Ni; thus, the light-gray area was neither pure carbides nor pure NiCr binder phase (Figure 6a and b). At the medium-gray mixture area for MC, some dark-gray nanometric particles dispersing into the light-gray area are observed (the rectangle ③ in Figure 5d). EDS spectra reveal a composition of C, O, Cr, Ni, and REO in this area (Figure 6e).

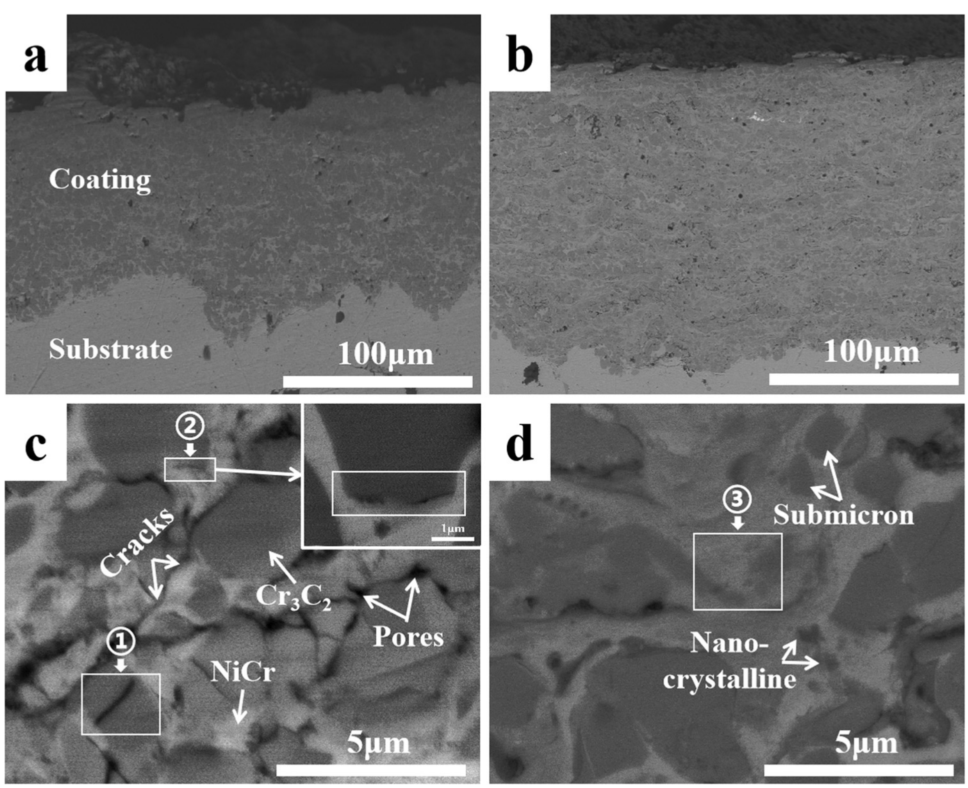

Figure 5: Cross-sectional SEM images of Cr_3C_2–NiCr coatings: (a and c) CC and (b and d) MC.

Meanwhile, submicron-sized and micron-sized Cr_3C_2 grains are distributed uniformly in the coatings, i.e., the multimodal distribution. Compared with CC, MC was observed in a higher uniform and higher dense microstructure. MC exhibits lower porosity (0.3 ± 0.12%) than that of CC (2.45 ± 0.15%; Figure 6f). Disparity in the coating microstructures is influenced by original powder morphology. This higher uniformity and density of MC depend on the structural characteristics of MP (i.e., homogenous and dense microstructures). The aforementioned process results in the complex microstructure, i.e., nonequilibrium phase, varying contrast scale, and different carbides content, of the multimodal coating.

For a further detailed analysis of the microstructural information of MC, the TEM bright-field image and corresponding selected area electron diffraction (SAED) patterns are shown in Figure 7. The single crystalline including Cr_3C_2, $Cr_{23}C_6$, and Cr_7C_3 crystals was observed with high magnification image and diffraction, which are marked as A, B, and C in Figure 7, respectively, which were consistent with the XRD results. The growth orientation of Cr_3C_2 crystal in SAED patterns was exactly consistent with the orientation facets [102] of the Cr_3C_2 crystalline structure, the growth orientation of $Cr_{23}C_6$ crystal in SAED patterns was exactly consistent with the orientation facets $[1\bar{1}\bar{1}]$ of the $Cr_{23}C_6$ single crystalline, and the growth orientation of Cr_7C_3 crystal in SAED patterns was exactly consistent with the Cr_7C_3 single-crystalline of zone axis $[0\bar{1}\bar{3}]$.

A few discontinuous elongated amorphous phases was clearly marked as D in Figure 7 and the diffraction pattern demonstrated diffuse rings. The elongated amorphous phases were randomly distributed in MC. The amorphous phase formation mainly are correlated to the nonequilibrium solidification processes of the NiCr binder. It is demonstrated that the multiple crystalline phases constituted of Cr_3C_2, Cr_7C_3, $Cr_{23}C_6$, and NiCr, which are marked E in Figure 7. Those multiple crystalline phases constituted multiple crystal forms with different dimensions, shapes, and orientations, thereby producing multiple types of diffraction spots and even diffraction rings.

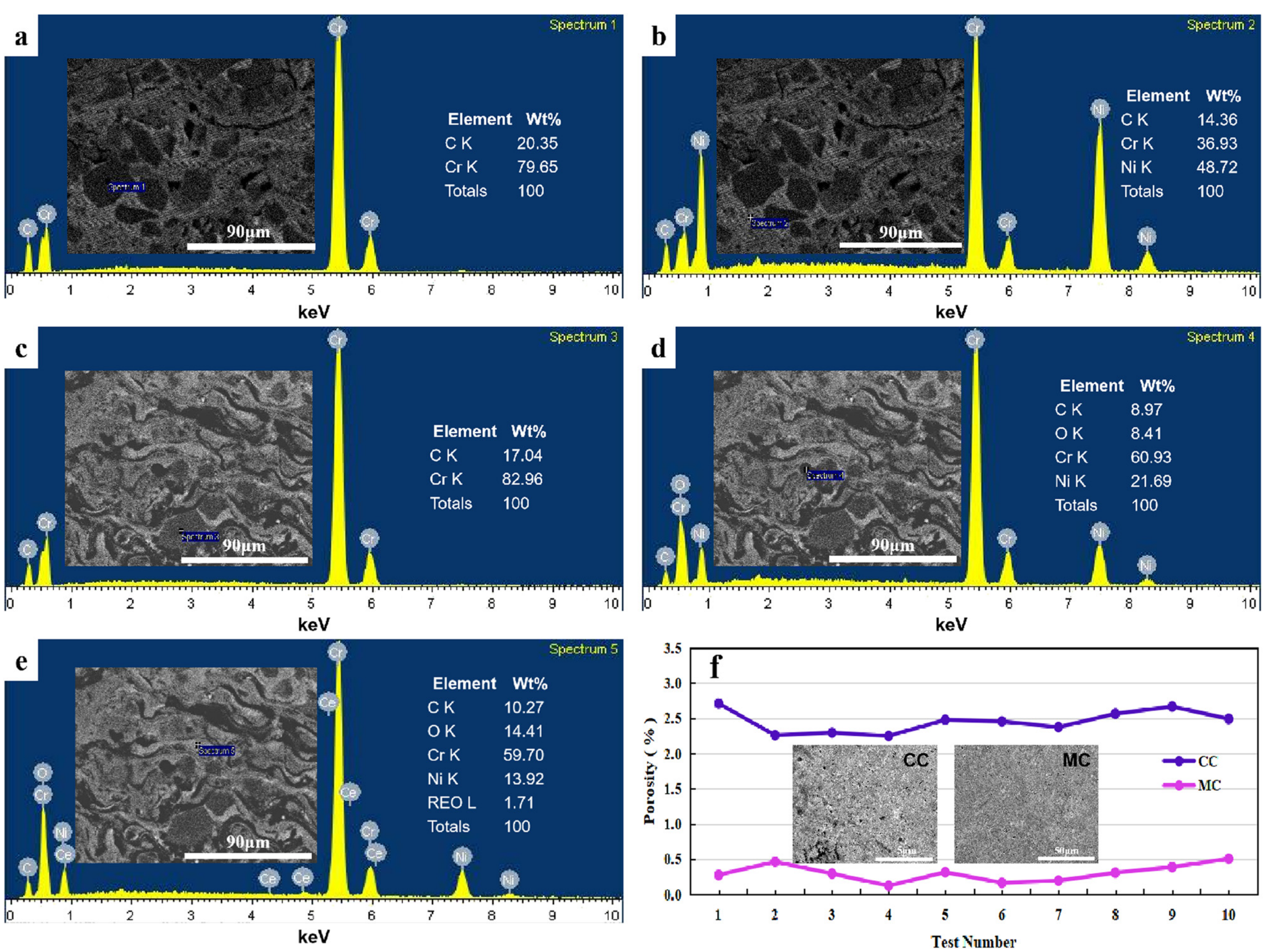

Figure 6: EDS spectra and porosity of the cross-sectional coatings: (a and b) EDS spectra of CC, (c–e) EDS spectra of MC, and (f) porosity.

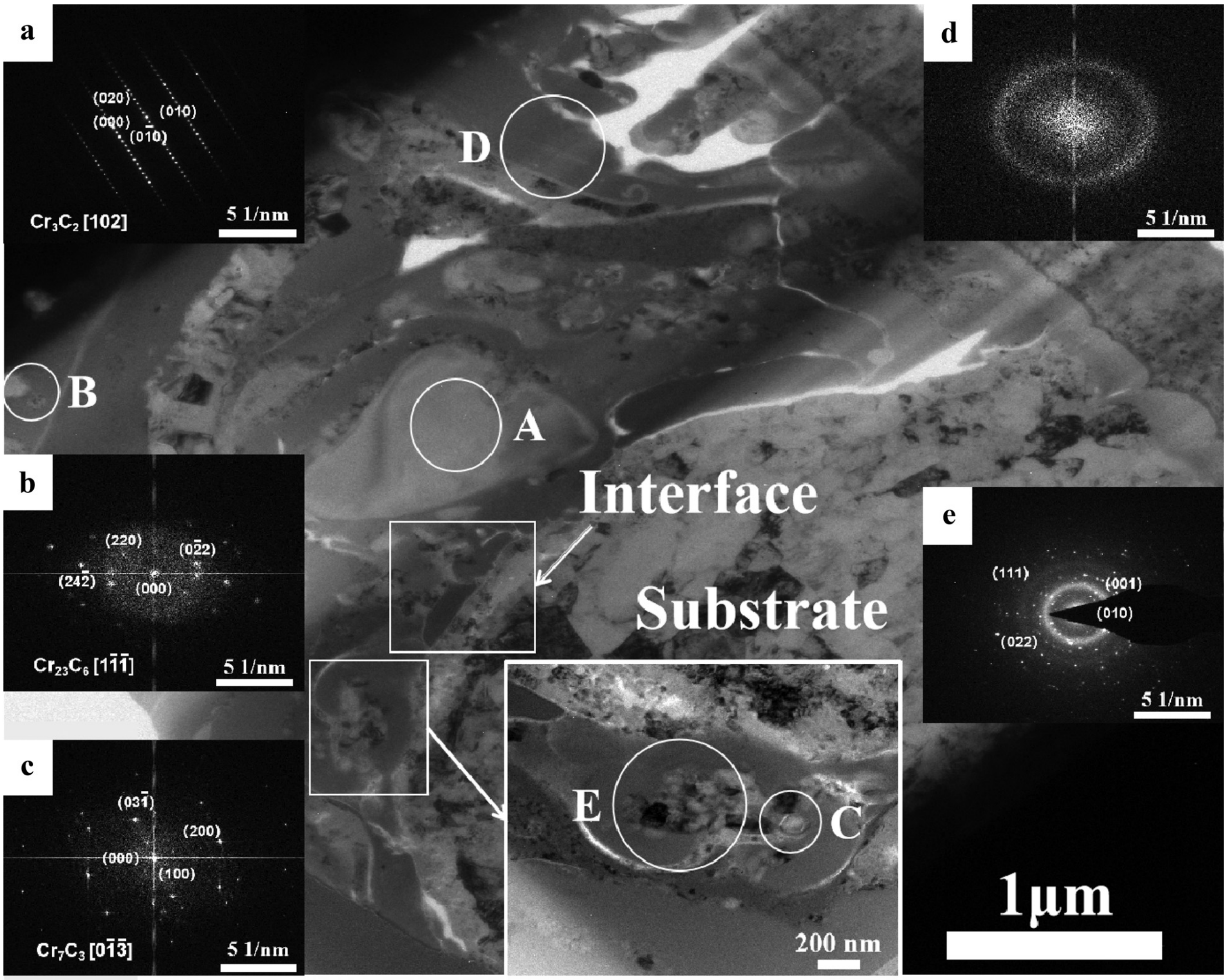

Figure 7: TEM micrograph and diffraction spot patterns of the cross-sectional MC. (a) Cr_3C_2, (b) $Cr_{23}C_6$, (c) Cr_7C_3, (d) amorphous phase, (e) multiple crystalline phase.

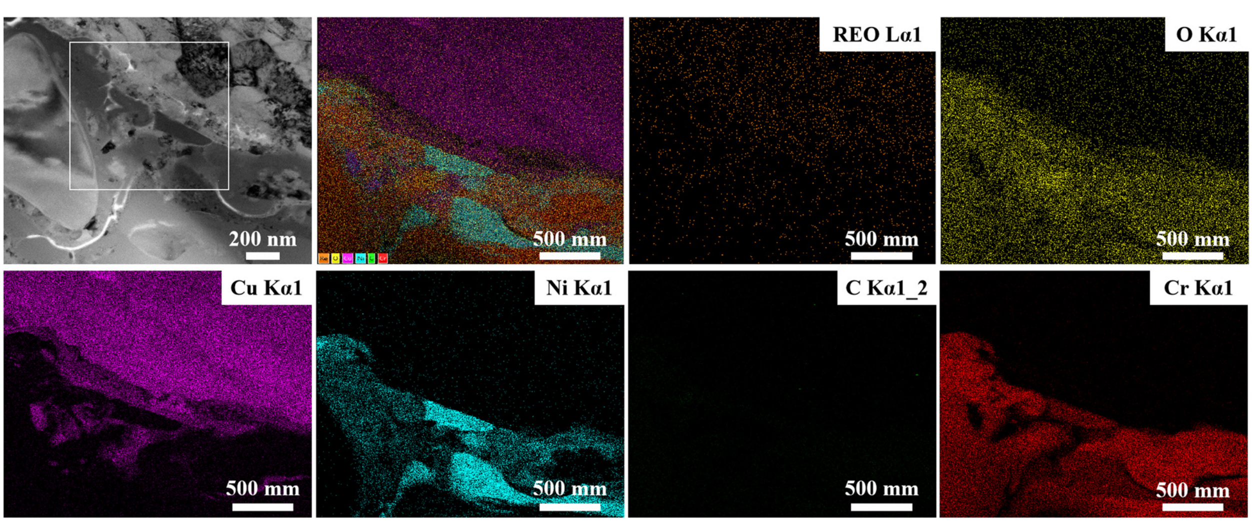

Figure 8: TEM micrograph and EDS elemental mapping for MC interface.

This reveals once again that carbide nanocrystalline grains with dimensions varying from 25 to 180 nm existed in the MC microstructure.

Figure 8 depicts the TEM bright field imaging and the EDS elemental mapping of the interface in Figure 7. According to EDS elemental mapping, the interface is mainly composed of REO, O, Cu, Ni, C, and Cr, and this is attributed to the interdiffusion of the coating and substrate. The observation of interfacial formations suggests that mechanical interlocking is the dominant bonding mechanism accompanied by local metallurgical bonds.

3.3 Mechanical properties of Cr_3C_2–NiCr coatings

Figure 9 shows the average values of microhardness and adhesive strength for both CC and MC. As shown in Figure 9a, MC had higher Vickers microhardness (985.85 ± 89.36 $HV_{0.3}$) compared with CC (837.19 ± 70.12 $HV_{0.3}$), taken on the cross section. The adhesive strength of MC (75.32 ± 1.21 MPa) significantly improved compared to CC (45.59 ± 1.03 MPa) and exhibited a 65 pct increase (Figure 9b). The good values of microhardness and adhesive strength of the multimodal coatings might be attributed to dispersion distribution and synergistic coupling effects of carbide grains with different scales. Owing to the advantages of HVOF technology (i.e., high velocity and low temperature), more nano-scale carbide grains embedded into the multimodal structure coating during deposition. According to the Hall–Petch relationship, the smaller grains have resulted in coatings with the larger microhardness [38]. In addition, the sub-micro scale or micro scale carbide grains would tend to interrupt or change crack path propagation, which would enhance toughness of the multimodal coatings [20,39]. The crack arresting effect shows that the mechanical properties of multimodal coatings are better than the conventional ones. For the conventional coatings, the crack tends to propagate along splat boundaries due to the weak inter-splat adhesion. For the multimodal coatings, the inter-splat adhesion is generally better and the coating is rather homogeneous; thus, crack propagation is limited [32].

3.4 Depositing mechanism of nano-modified multimodal structure Cr_3C_2–NiCr coatings

For a better description of the mechanism of the multimodal structure coating formation, four stages are schematically shown in Figure 10:

In the study, a single nano-modified multimodal Cr_3C_2–NiCr particle is used as a starting material.

(a) **In a solid state.** As mentioned earlier, multimodal Cr_3C_2–NiCr particle is an agglomerated material, which consists of coarse (micron and submicron) and fine (nano) Cr_3C_2 grains and NiCr binder phases. It forms a three-layer structure: a multiscale chromium and nickel carbide cermet core with a metal binder shell, which was covered by submicron and nano chromium carbide particles and rare earth oxide additives (see Figure 10a).

(b) **Molten.** However, grains of three different sizes have different melting degrees when passing through the flame in the HVOF gun. The melting of the original particle exhibits a strong dependency on the spray temperature and the grain size distribution. In the

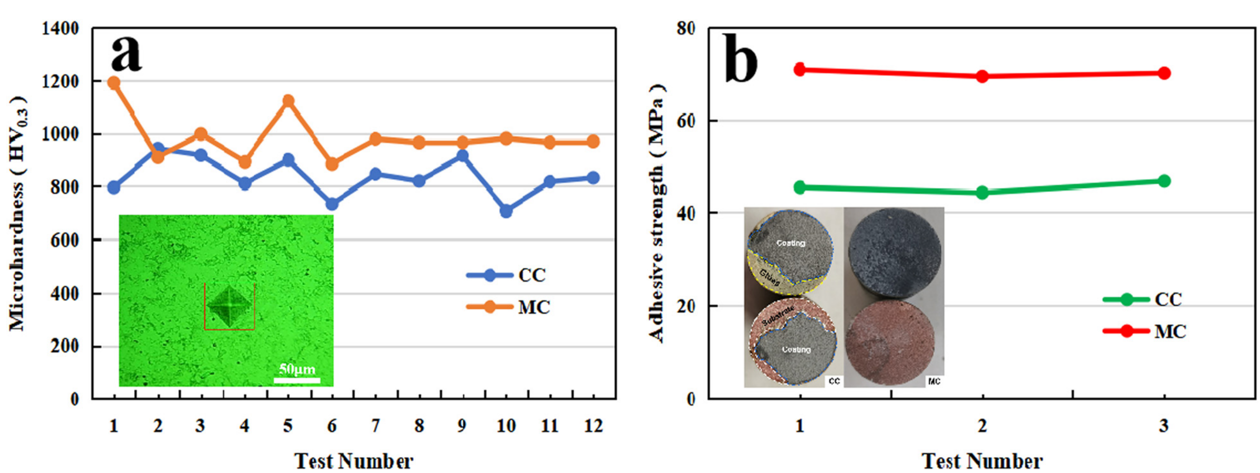

Figure 9: Microhardness and adhesive strength of the Cr_3C_2–NiCr coatings. (a) Microhardness, (b) adhesive strength.

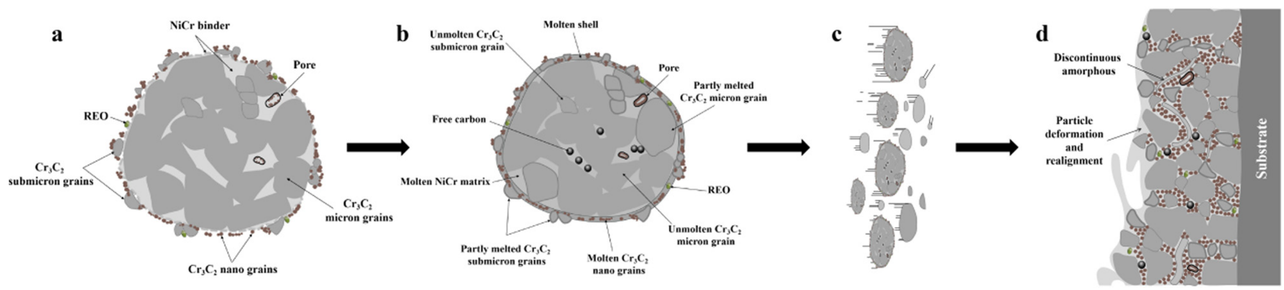

Figure 10: Schematic of the formation of the multimodal structure coatings: (a) original particle, (b) molten part of the particle, (c) particle deformation, and (d) cross section of the multimodal coatings.

case of the short dwell time in the HVOF jet and when the temperature is low enough (not significantly higher than the melting temperature of the original powder), the NiCr binder phases will fully melt. The nano Cr_3C_2 grains adhering to the surface will melt with relative ease, leading to dissolving rapidly in the binder phases. While the submicron and micron Cr_3C_2 grains in the inner core (melting point of 2200 K) will remain partially melted or unmelted, but softened by heating (see Figure 10b).

(c) **Deformation.** The particles in a molten state are flattened upon impact and due to quench and solidification, resulting in splats. While particles in the partly melted or unmelted state were plastic deformation at impact, and their consolidations were due to the shot peening effect of the new incoming particles [32] (see Figure 10c).

(d) **Realignment.** The particles realign after quenching on the substrate. The coating cross section exhibits a dense coating (see Figure 10d). The different sizes of Cr_3C_2 grains are uniformly distributed throughout the coating microstructure, half-melted or unmolten submicron Cr_3C_2 grains filled in the voids formed by only the heated and softened micron Cr_3C_2 grains, fully molten NiCr binder phases and nano Cr_3C_2 grains provide a strong and tough matrix in which the micron and submicron grains embed and be held in place [40], and nano Cr_3C_2 grains are dispersed in NiCr binder phases [27].

The final microstructure of the nano-modified Cr_3C_2–NiCr coating is characterized by a "multimodal structure," which is similar to concrete construction, formed by nano-sized, submicron-sized, and micron-sized hard phases and metallic binder phases. The micron-sized and submicron-sized hard phases are analogous to gravel and sand in concrete, respectively, and the nano-sized hard phases and metallic binder phases act as "cement" [26].

4 Conclusions

In conclusion, nano-modified multimodal and conventional structure Cr_3C_2–NiCr coatings were deposited on CuCrZr by HVOF thermal spraying. The microstructure and mechanical properties of both coatings were comparatively studied. Besides, the depositing mechanism of the nano-modified multimodal structure Cr_3C_2–NiCr coatings have been described in detail. The main conclusions are presented as follows:

1. A single nano-modified multimodal Cr_3C_2–NiCr particle consisted of 11.5 wt% nano grains (25–180 nm), 34.6% sub-micro grains (200 nm to 0.5 μm), and 53.9% micro grains (2–4.5 μm). It forms a three-layer structure: a multimodal chromium and nickel carbide cermet core with a metal binder shell, which were covered by submicron and nano chromium carbide particles and rare earth oxide additives.
2. The multimodal Cr_3C_2–NiCr coatings are formed by nano-sized, submicron-sized, and micron-sized hard grains and metallic binder phases. Submicron Cr_3C_2 grains embedded in the voids formed by micron Cr_3C_2 grains, NiCr binder phases, and nano Cr_3C_2 grains imbedded in the voids formed by submicron and micron Cr_3C_2 grains, and nano Cr_3C_2 grains are dispersed in NiCr metal binder phases. A few discontinuous elongated amorphous and nanocrystalline phases existed in them.
3. Compared with the conventional Cr_3C_2–NiCr coating, the multimodal Cr_3C_2–NiCr coating is uniform and dense as well as not obvious lamellar structures, and the porosity is only 0.3 ± 0.12%.
4. The microhardness increased from 837.19 ± 70.12 $HV_{0.3}$ for the conventional Cr_3C_2–NiCr coating to 985.85 ± 89.36 $HV_{0.3}$ for the multimodal Cr_3C_2–NiCr coating. The adhesive strength for MC (75.32 ± 1.21 MPa) significantly increased to 65%, compared with CC (45.59 ± 1.03 MPa).

5. In consideration of the fact that the copper crystallizer, the core component of continuous casting equipment in the steel industry is mainly used as the working layers by electrolytic hard chromium coatings, which show poor performance, short life span, and serious environmental pollution and harmful effects on public health (hexavalent chromium). The nano-modified multimodal structure Cr_3C_2–NiCr coatings prepared on copper crystallizer by HVOF spraying, which have high spraying efficiency, high hardness and adhesive strength, low porosity, and low costs, are significantly attractive for the gains in copper crystallizer performance, superior lifetime, and the pollution reduction. Therefore, the multimodal Cr_3C_2–NiCr coatings would be the most important replacement for hard chromium electroplating coatings.

Acknowledgments: The authors are grateful to the valuable help from professor Wang You of the Harbin University of Technology of China, the support from Jiamusi University College of Materials Science and Engineering and Metal Wear Resistant Materials and Surface Technology Engineering Research Center in the Ministry of Education of China.

Funding information: The work was supported by the National Natural Science Foundation of China (grant No. 51671096).

Author contributions: Ming Hu contributed significantly to designed the conception of the study and conducted final approval of manuscript; Chenxi Shi performed the research, analyzed and interpreted the collected data, and wrote the manuscript; Shibin Liu and Qinglin Gong performed the experiment; Irfan and Huan Wang contributed to carrying out additional analyses with constructive discussions.

Conflict of interest: We declare that we have no conflict of interest with other people or organizations.

Data availability statement: The datasets generated during and/or analysed during the current study are available from the corresponding author on reasonable request.

References

[1] Hao, E., Y. An, X. Liu, Y. Wang, H. Zhou, and F. Yan. Effect of annealing treatment on microstructures, mechanical properties and cavitation erosion performance of high velocity oxy-fuel sprayed NiCoCrAlYTa coating. *Journal of Materials Science & Technology*, Vol. 53, 2020, pp. 19–31.

[2] Ghadami, F. and A. S. R. Aghdam. Improvement of high velocity oxy-fuel spray coatings by thermal post-treatments: A critical review. *Thin Solid Films*, Vol. 678, 2019, pp. 42–52.

[3] Kilic, H. and C. Misirli. Research on tribological behavior of Cr_3C_2-25NiCr-coated brake disc. *Surface Review and Letters*, Vol. 28, No. 10, 2021. id. 2150097.

[4] Liu, X., X. Zhao, and F. Yang. Room-temperature and high-temperature wear behaviors of as-sprayed and annealed Cr_3C_2-25NiCr coatings prepared by high velocity air-fuel spraying. *Coatings*, Vol. 10, No. 11, 2020, id. 1090.

[5] Vashishtha, N. and S. G. Sapate. Abrasive wear maps for High Velocity Oxy Fuel (HVOF) sprayed WC-12Co and Cr_3C_2-25NiCr coatings. *Tribology International*, Vol. 114, 2017, pp. 290–305.

[6] Lu, H., J. Shang, X. Jia, Y. Li, F. Li, J. Li, et al. Erosion and corrosion behavior of shrouded plasma sprayed Cr_3C_2-NiCr coating. *Surface & Coatings Technology*, Vol. 388, 2020, id. 388.

[7] Shi, M., Z. Xue, H. Liang, Z. Yan, X. Liu, and S. Zhang. High velocity oxygen fuel sprayed Cr_3C_2-NiCr coatings against Na_2SO_4 hot corrosion at different temperatures. *Ceramics International*, Vol. 46, No. 15, 2020, pp. 23629–23635.

[8] Brown, R. F., G. M. Smith, A. Hehr, and T. J. Eden. Ultrasonic consolidation post-treatment of CuNi: Cr_3C_2-NiCr composite cold spray coatings: A mechanical and microstructure assessment. *Journal of Thermal Spray Technology*, Vol. 30, No. 8, 2021, pp. 2069–2082.

[9] Dzhurinskiy, D., A. Babu, P. Pathak, A. Elkin, S. Dautov, and P. Shornikov. Microstructure and wear properties of atmospheric plasma-sprayed Cr_3C_2-NiCr composite coatings. *Surface & Coatings Technology*, Vol. 428, 2021, id. 428.

[10] Janka, L., J. Norpoth, R. Trache, S. Thiele, and L. M. Berger. HVOF- and HVAF-Sprayed Cr_3C_2-NiCr coatings deposited from feedstock powders of spherical morphology: Microstructure formation and high-stress abrasive wear resistance up to 800 degrees C. *Journal of Thermal Spray Technology*, Vol. 26, No. 7, 2017, pp. 1720–1731.

[11] Schwanekamp, T., G. Marginean, and M. Reuber. Laser beam melting of Cr_3C_2-NiCr. *International Journal of Refractory Metals & Hard Materials*, Vol. 85, 2019, id. 85.

[12] Zhang, Y., K. Chong, Q. Liu, Y. Bai, Z. Zhang, D. Wu, et al. High-temperature tribological behavior of thermally-treated supersonic plasma sprayed Cr_3C_2-NiCr coatings. *International Journal of Refractory Metals & Hard Materials*, Vol. 95, 2021, id. 95.

[13] Ahuja, L., D. Mudgal, S. Singh, and S. Prakash. A comparative study to evaluate the corrosion performance of Zr incorporated Cr_3C_2-(NiCr) coating at 900 degrees C. *Ceramics International*, Vol. 44, No. 6, 2018, pp. 6479–6492.

[14] Goyal, K. and R. Goyal. Improving hot corrosion resistance of Cr_3C_2-20NiCr coatings with CNT reinforcements. *Surface Engineering*, Vol. 36, No. 11, 2020, pp. 1200–1209.

[15] Mahade, S., A. Mulone, S. Björklund, U. Klement, and S. Joshi. Novel suspension route to incorporate graphene nano-platelets in HVAF-sprayed Cr_3C_2-NiCr coatings for superior wear performance. *Journal of Materials Research and Technology-Jmr&T*, Vol. 13, 2021, pp. 498–512.

[16] Saladi, S., J. Menghani, and S. Prakash. Effect of CeO_2 on cyclic hot-corrosion behavior of detonation-gun sprayed Cr_3C_2-NiCr

coatings on ni-based superalloy. *Journal of Materials Engineering and Performance*, Vol. 24, No. 3, 2015, pp. 1379–1389.
[17] Matthews, S., M. Bhagvandas, and L.-M. Berger. Creation of modified Cr_3C_2-NiCr hardmetal coating microstructures through novel processing. *Journal of Alloys and Compounds*, Vol. 824, 2020, id. 824.
[18] He, J. H., M. Ice, and E. J. Lavernia. Synthesis of nanostructured Cr_3C_2-25(Ni20Cr) coatings. *Metallurgical and Materials Transactions a-Physical Metallurgy and Materials Science*, Vol. 31, No. 2, 2000, pp. 555–564.
[19] Picas, J. A., A. Forn, A. Igartua, and G. Mendoza. Mechanical and tribological properties of high velocity oxy-fuel thermal sprayed nanocrystalline CrC-NiCr coatings. *Surface & Coatings Technology*, Vol. 174, 2003, pp. 1095–1100.
[20] Fauchais, P., G. Montavon, R. S. Lima, and B. R. Marple. Engineering a new class of thermal spray nano-based microstructures from agglomerated nanostructured particles, suspensions and solutions: an invited review. *Journal of Physics D-Applied Physics*, Vol. 44, No. 9, 2011, id. 093001.
[21] Fu, Q., P. Zhang, L. Zhuang, L. Zhou, J. Zhang, J. Wang, et al. Micro/nano multiscale reinforcing strategies toward extreme high-temperature applications: Take carbon/carbon composites and their coatings as the examples. *Journal of Materials Science & Technology*, Vol. 96, 2022, pp. 31–68.
[22] Ding, X., X. Cheng, X. Yu, C. LI, C. Yuan, and Z. Ding. Structure and cavitation erosion behavior of HVOF sprayed multi-dimensional WC-10Co4Cr coating. *Transactions of Nonferrous Metals Society of China*, Vol. 28, No. 3, 2018, pp. 487–494.
[23] Ji, G.-C., H.-T. Wang, X. Chen, X.-B. Bai, Z.-X. Dong, and F.-G. Yang. Characterization of cold-sprayed multimodal WC-12Co coating. *Surface & Coatings Technology*, Vol. 235, 2013, pp. 536–543.
[24] Mi, P., T. Wang, and F. Ye. Influences of the compositions and mechanical properties of HVOF sprayed bimodal WC-Co coating on its high temperature wear performance. *International Journal of Refractory Metals & Hard Materials*, Vol. 69, 2017, pp. 158–163.
[25] Poblano-Salas, C. A., J. A. Cabral-Miramontes, A. Gallegos-Melgar, H. Ruiz-Luna, J. D. Aguilar-Escobar, D. G. Espinosa-Arbelaez, et al. Effects of VC additions on the mechanical properties of bimodal WC-Co HVOF thermal sprayed coatings measured by nanoindentation. *International Journal of Refractory Metals & Hard Materials*, Vol. 48, 2015, pp. 167–178.
[26] Sun, X., J. Huang, J. Yang, and S. Chen. Microstructure evolution and mechanical properties of in-situ bimodal TiC-Fe coatings prepared by reactive plasma spraying. *Ceramics International*, Vol. 45, No. 5, 2019, pp. 5848–5857.
[27] Vereschaka, A., S. Grigoriev, V. Tabakov, M. Migranov, N. Sitnikov, F. Milovich, et al. Influence of the nanostructure of Ti-TiN-(Ti, Al, Cr)N multilayer composite coating on tribological properties and cutting tool life. *Tribology International*, Vol. 150, 2020, id. 150.
[28] Wang, X., T. Ouyang, X. Duan, C. Ke, X. Zhang, J. Min, et al. Improved solar absorptance of WC/Co solar selective absorbing coating with multimodal WC particles. *Metals*, Vol. 7, No. 4, 2017, id. 137.
[29] Qi, N., S. Liao, J. Li, C. Wu, M. Lv, Y. Liu, et al. Quantitative characterization of carbide loss and correlation with microstructure and performance of plasma-sprayed NiCr-Cr_3C_2 metal carbide coatings. *Journal of Thermal Spray Technology*, Vol. 30, No. 1–2, 2021, pp. 457–470.
[30] Ding, Y., T. Hussain, and D. G. Mccartney. High-temperature oxidation of HVOF thermally sprayed NiCr-Cr_3C_2 coatings: microstructure and kinetics. *Journal of Materials Science*, Vol. 50, No. 20, 2015, pp. 6808–6821.
[31] Ghadami, F., A. S. R. Aghdam, and S. Ghadami. A comprehensive study on the microstructure evolution and oxidation resistance of conventional and nanocrystalline MCrAlY coatings. *Scientific Reports*, Vol. 11, No. 1, 2021, id. 875.
[32] Fauchais, P., J. V. R. Heberlein, M. Boulos. Thermal spray fundamentals. *From Powder to Part*, SPRINGER, 2013, p. 1566.
[33] Guilemany, J. M., J. M. Miguel, S. Vizcaıno, C. Lorenzana, J. Delgado, and J. Sanchez. Role of heat treatments in the improvement of the sliding wear properties of Cr3C2-NiCr coatings. *Surface & Coatings Technology*, Vol. 157, No. 2–3, 2002, pp. 207–213.
[34] Chandra, S. and P. Fauchais. Formation of solid splats during thermal spray deposition. *Journal of Thermal Spray Technology*, Vol. 18, No. 2, 2009, pp. 148–180.
[35] Robertson, A. L. and K. W. White. Microscale fracture mechanisms of a Cr_3C_2-NiCr HVOF coating. *Materials Science and Engineering a-Structural Materials Properties Microstructure and Processing*, Vol. 688, 2017, pp. 62–69.
[36] Matthews, S., A. Asadov, S. Ruddell, and L. M. Berger. Thermally induced metallurgical processes in Cr_3C_2-NiCr thermal spray coatings as a function of carbide dissolution. *Journal of Alloys and Compounds*, Vol. 728, 2017, pp. 445–463.
[37] Wang, Y., Y. Bai, K. Wu, J. Zhou, M. G. Shen, W. Fan, et al. Flattening and solidification behavior of in-flight droplets in plasma spraying and micro/macro-bonding mechanisms. *Journal of Alloys and Compounds*, Vol. 784, 2019, pp. 834–846.
[38] Pakdel, A., A. Witecka, G. Rydzek, and D. N. Awang Shri. A comprehensive microstructural analysis of Al-WC micro- and nano-composites prepared by spark plasma sintering. *Materials and Design*, Vol. 119, 2017, pp. 225–234.
[39] Lima, R. S. and B. R. Marple. Thermal Spray coatings engineered from nanostructured ceramic agglomerated powders for structural, thermal barrier and biomedical applications: a review. *Journal of Thermal Spray Technology*, Vol. 16, 2007, pp. 40–63.
[40] Skandan, G., R. Yao, R. Sadangi, B. H. Kear, Y. Qiao, L. Liu, et al. Multimodal coatings: A new concept in thermal spraying. *Journal of Thermal Spray Technology*, Vol. 9, No. 3, 2000, pp. 329–331.